Tides on the West Florida Shelf

RUOYING HE AND ROBERT H. WEISBERG

College of Marine Science, University of South Florida, St. Petersburg, Florida

(Manuscript received 3 October 2001, in final form 22 May 2002)

ABSTRACT

The principal semidiurnal (M_2 and S_2) and diurnal (K_1 and O_1) tidal constituents are described on the west Florida continental shelf (WFS) using a combination of in situ measurements and a three-dimensional, primitive equation numerical model. The measurements are of sea level and currents along the coastline and across the shelf, respectively. The model extends from west of the Mississippi River to the Florida Keys with an open boundary arcing between. It is along this open boundary that the regional model is forced by a global tide model. Standard barotropic tidal analyses are performed for both the data and the model, and quantifiable metrics are provided for comparison. Based on these comparisons, the authors present coamplitude and cophase charts for sea level and velocity hodographs for currents. The semidiurnal constituents show marked spatial variability, whereas the diurnal constituents are spatially more uniform. Apalachicola Bay is a demarcation point for the semidiurnal tides that are well developed to the southeast along the WFS but are minimal to the west. The largest semidiurnal tides are in the Florida Big Bend and Florida Bay regions with a relative minimum in between just to the south of Tampa Bay. These spatial distributions may be explained on the basis of local geometry. A Lagrangian Stokes drift, coherently directed toward the northwest, is identified but is of relatively small magnitude when compared with the potential for particle transport by seasonal and synoptic-scale forcing. Bottom stress-induced tidal mixing is examined and estimates are made of the bottom logarithmic layer height by the M_2 tidal currents.

1. Introduction

The Gulf of Mexico is a semienclosed basin connected to the Atlantic Ocean by the Straits of Florida and to the Caribbean Sea by the Yucatan Channel. A notable feature of the Gulf of Mexico tides as compared with other places around the world is a dominance of the diurnal over the semidiurnal constituents (Reid and Whitaker 1981). This is in contrast with the east coast of the United States, where the tides are predominantly semidiurnal (Zetler and Hansen 1971). Previous Gulf of Mexico tides studies concluded that the diurnal tide is primarily co-oscillating, entering the Gulf of Mexico through the Straits of Florida and exiting through the Yucatan Channel. (Grace 1932; Zetler and Hansen 1971).

Located on the eastern side of the Gulf of Mexico, the west Florida continental shelf (WFS) is one of North America's broadest continental shelves. Apparently different from most of the Gulf of Mexico basin, semidiurnal tides are appreciable here. Although this tidal structure was discussed in previous studies (Clarke 1991; Reid and Whitaker 1981), descriptions of WFS tides are limited to coastal sea level and a few regional current measurements. Koblinsky (1981) described the M_2 tide over the southern portion of the WFS using velocity measurements from five moorings over a 2-yr duration. The surface wave crests of the M_2 tide, considered to be stationary, linear, and barotropic, were found to parallel the isobaths. Internal tides were not found and the temperature distribution was only slightly distorted by the surface wave. Marmorino (1983) added analyses of velocity data from four moorings deployed in the Florida Big Bend region. Semidiurnal tidal constituent (M_2 and S_2) energy was found to decrease in the offshore direction, whereas the diurnal tidal constituent (K_1 and O_1) energy was more uniform across the shelf. As a result, the characterization of the tidal fluctuations changes from predominantly diurnal in deep water to semidiurnal near the coast. Such spatial inhomogeneity exists throughout the WFS. Weisberg et al. (1996) using velocity data from the 47-m isobath, showed that particle displacements in the semidiurnal and diurnal bands are typically about 1 km. However, inertial oscillations, during months when the water column is stratified, can cause an increase in the diurnal band particle excursions to about 5 km.

A deficiency of moored current meter data alone is that realistic arrays are insufficient to map the tides over the entire WFS. To do this we need a combination of

Corresponding author address: Ruoying He, College of Marine Science, University of South Florida, 140 7th Avenue South, St. Petersburg, FL 33701.
E-mail: ruoying@marine.usf.edu

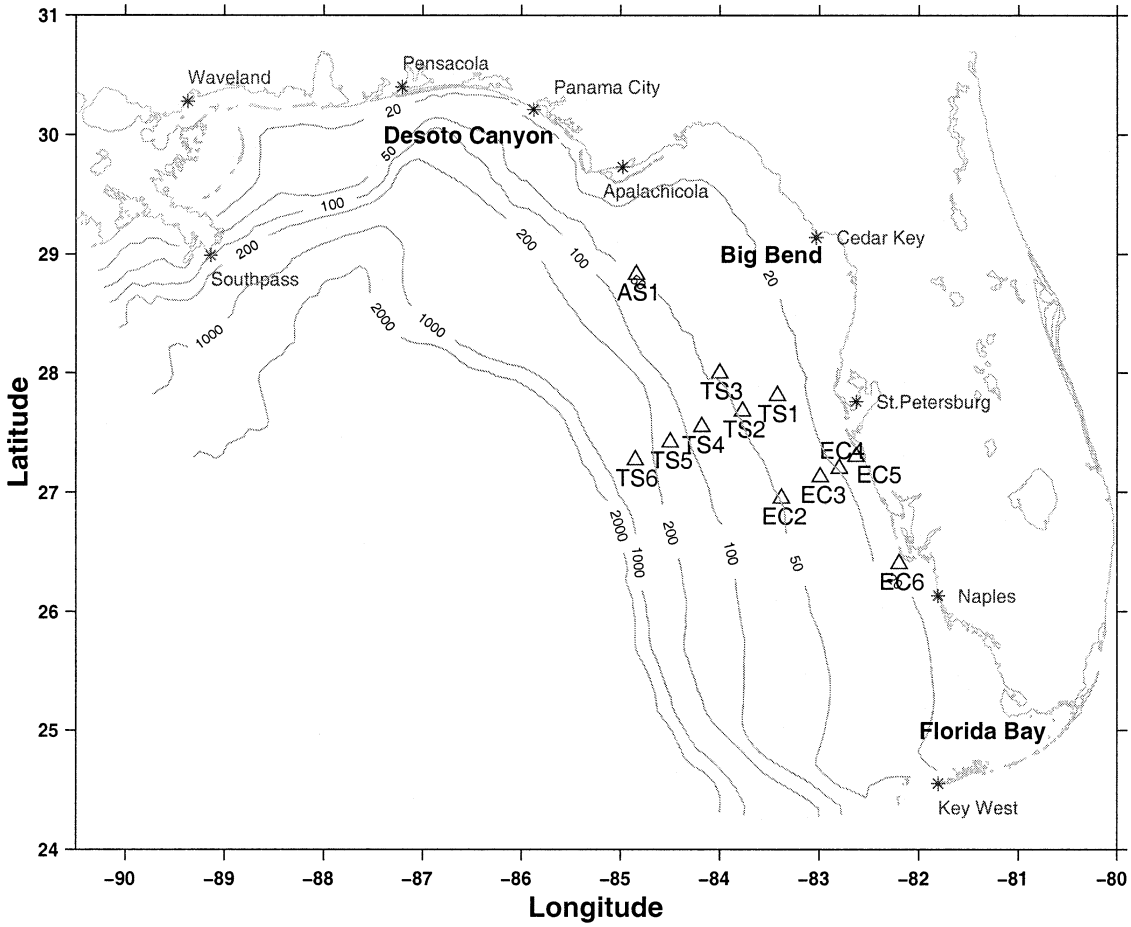

FIG. 1. Model domain and observational locations. The nine tide gauges (denoted by asterisks) are South Pass, Waveland, Pensacola, Panama City, Apalachicola, Cedar Key, St. Petersburg, Naples, and Key West. The 12 moorings for velocity data (denoted by open triangles) are AS1 (47 m), TS1 (31 m), TS2 (47 m), TS3 (46 m), TS4 (63 m), TS5 (142 m), TS6 (296 m), EC2 (50 m), EC3 (30 m), EC4 (20 m), EC5 (10 m), and EC6 (10 m).

in situ data and a high-resolution, area-encompassing model. The present paper combines recent in situ measurements with a three-dimensional, primitive equation numerical model to describe and map the four major tidal constituents (M_2, S_2, K_1, and O_1) on the shelf from the Florida Keys to the Mississippi River. We concentrate on the barotropic tides since the baroclinic tides are seasonally modulated and an order of magnitude smaller. Exceptions to the baroclinic motions being relatively small are seasonally modulated inertial oscillations whose frequency overlaps with the diurnal tides. Baroclinic tides and inertial oscillations, whose effects on the deterministic barotropic tides are negligible (Clarke 1991), will be the subject of a future correspondence.

We begin in section 2 with the observations of coastal sea level and shelfwide currents, analyzing the barotropic tides by standard methods. Section 3 then introduces the regional model and discusses how it is driven at the open boundary by deep-ocean barotropic tides. The modeled tides and their comparisons with the in situ data for the M_2, S_2, K_1, and O_1 constituents are described in section 4. Based on these comparisons we provide maps of the principal constituent tidal ellipses over the entire domain using the model. We also use the model to estimate the Lagrangian transports induced by the barotropic tides and their attendant nonlinear interactions. Since the amplitude of the tides determines their contribution to turbulent mixing, this is a topic of discussion in section 5. The results are summarized in section 6.

2. Observations

The in situ observations are taken from nine tide gauges operated by NOAA National Ocean Service (NOS) and 12 current meter moorings deployed by the University of South Florida (Fig. 1). The nine tide gauges, referred to as South Pass, Waveland, Pensacola, Panama City, Apalachicola, Cedar Key, St. Petersburg, Naples, and Key West span the northeast Gulf of Mexico from the Mississippi River to the Florida Keys. The

velocity data are from acoustic Doppler current profilers deployed across the WFS between the 300-m and 10-m isobaths.

a. Tidal height

The sea level data are analyzed using the least squares error method of Foreman and Henry (1979). The analysis includes as many as 146 possible tidal constituents, 45 of these being astronomical in origin and the remaining 101 being shallow water constituents (e.g., Godin 1972) that arise by distortions of the astronomical tidal constituents due to the nonlinear effects of shoaling depth. Year-long time series of sea level are used for each of the nine sea level station analyses inclusive of the years 1996–99. Data gaps preclude using the same year for all stations. Table 1 lists the amplitudes and phases (relative to the Greenwich meridian) for the M_2, S_2, K_1, and O_1 constituents, which in sum contain over 90% of the tidal variance. We note that the semidiurnal tides to the south of are larger than those west of Apalachicola Bay. In contrast with the diurnal tides that have similar amplitudes at all nine stations, the semidiurnal tides show large spatial variations. All of the four major constituents have amplitudes that peak near Cedar Key.

To quantify the contribution that the tides make to the total sea level variance, a predicated tidal height time series, ζ_p, is constructed by adding the four major tidal constituents. With ζ_0 being the observed sea surface height time series after removing the mean, the root-mean-square tidal residual (i.e., the subtidal component), σ_r, and the normalized residual, σ_r/σ_0, where σ_0 is the standard deviation of ζ_0, are calculated over the time series record length, T, as

$$\sigma_r = \sqrt{\frac{1}{T}\int [\zeta_p(t) - \zeta_0(t)]^2\, dt}. \quad (1)$$

The ratios of the subtidal variability to the total sea level variability, σ_r/σ_0, are given as percentages in Table 2. We note that west of Apalachicola Bay, where the tides are generally small, the subtidal variability accounts for more than 70% of total variability. South of Apalachicola Bay, where the tides are larger, the tidal and the subtidal variabilities contribute about equally to the total sea level variability.

b. Tidal currents

In parallel with sea level the tidal analyses for the moored velocity data are performed using the least squares error method of Foreman (1978). Since the 12 mooring locations were generally not codeployed, the analysis intervals (between 1996 and 1999) differ in record length and time origin. We generally used the entire record length available at each site, and these varied from around three months to one year.

Parameters describing the tidal hodographs are calculated at each depth bin (from 0.5 to 10 m depending on water depth) for each mooring. The amplitudes of the ellipse semimajor axis and the ellipse orientations (measured anticlockwise from east) are shown as a function of depth in Figs. 2 and 3 for the four major constituents: M_2, S_2, O_1, and K_1. For a purely barotropic tide the amplitude and orientation would be independent of depth and appear as vertical lines. Depth profile deviations from straight lines are related to bottom friction, baroclinicity, contamination by inertial motions, or combinations of these. As shown in Fig. 2 for relatively shallow depths and in Fig. 3 for relatively deeper depths, the semidiurnal tides indeed appear to be barotropic, which agrees with the finding of Koblinsky (1981) for the WFS M_2 tide. In contrast, the diurnal tides, especially in deeper water, tend to show vertical structure. This is most likely due to contamination by inertial motions since in the central WFS the inertial period is about 25.90 h, which is close to the O_1 and K_1 periods of 25.82 and 23.93 h, respectively. WFS inertial oscillations are modulated in time along with the seasonally varying stratification (Weisberg et al. 1996), and they are evident in velocity component plots as baroclinic modes consistent with the orientation reversals seen for the deeper records in Fig. 3.

Overall, the observed tidal current amplitudes on the WFS are weak (on the order of a few centimeters per second). Of the principal constituents, the M_2 current is the strongest; its amplitude tends to increase shoreward, and its ellipse orientation tends to align perpendicular to the isobaths. While weaker, the diurnal constituent amplitudes are more uniformly distributed across the shelf, and these findings agree with those of Marmorino (1983) for the Florida Big Bend region.

c. Phases of tidal height and tidal currents

One question of interest (particularly for recreational fishermen) is the relative phase between the tidal height at the coast and the tidal currents on the WFS. We address this question relative to the St. Petersburg tide gauge, the reference gauge for much of the WFS, in two different ways. Table 3a shows the phases (and corresponding time lags) between high tide at St. Petersburg and maximum tidal currents (directed toward the coast) at the 12 ADCP mooring sites for each of the major tidal constituents. For the semidiurnal tides, the times of maximum tidal current generally lead the high tide at St. Petersburg by 2–9 h. On the other hand, the maximum tidal currents of the diurnal tide, lag the high tide time at St. Petersburg by 10–20 h.

A second approach is to construct time series of the tidal height at St. Petersburg and the tidal currents at the 12 ADCP sites by combining the four major tidal constituents, and then producing a set of lags for these composite time series. Table 3b gives these maximum correlation time lags between the water level η and the major component of tidal current u defined as

TABLE 1. Comparison of observed and computed tidal elevation at reference sites.

Station	Amplitude H (m $\times 10^{-2}$) Observed	Modeled	ΔH	Phase ϕ (°G) Observed	Modeled	$\Delta\phi$
			M_2			
South Pass	1.73	2.44	−0.71	116.65	123.75	−7.10
Waveland	2.78	4.05	−1.27	207.75	204.01	3.74
Pensacola	2.26	2.51	−0.25	171.48	165.59	5.89
Panama	2.74	3.01	−0.27	139.93	133.64	6.29
Apalachicola	11.64	13.37	−1.73	255.78	253.64	2.14
Cedar Key	37.31	39.78	−2.47	186.50	186.02	0.48
St. Petersburg	17.20	17.77	−0.57	198.10	200.66	−2.56
Naples	26.40	25.54	0.86	143.36	144.18	−0.82
Key West	18.60	17.51	1.09	66.90	67.17	−0.27
			S_2			
South Pass	1.06	1.02	0.04	108.40	110.92	−2.52
Waveland	2.24	2.31	−0.07	225.67	220.81	4.86
Pensacola	0.97	1.00	−0.03	159.36	156.96	2.40
Panama	1.20	1.17	0.03	142.23	135.20	7.03
Apalachicola	3.53	3.95	−0.42	278.28	278.52	−0.24
Cedar Key	10.79	11.57	−0.78	226.94	231.22	−4.28
St. Petersburg	5.40	6.28	−0.88	216.10	222.86	−6.76
Naples	8.89	7.89	1.00	162.15	167.12	−4.97
Key West	5.20	4.12	1.08	88.24	86.07	2.17
			O_1			
South Pass	13.83	11.50	2.33	8.56	9.57	−1.01
Waveland	15.85	15.63	0.22	48.62	47.25	1.37
Pensacola	13.49	13.58	−0.09	42.80	39.73	3.07
Panama	13.65	12.75	0.90	27.60	21.20	6.40
Apalachicola	11.46	12.27	−0.81	45.70	44.35	1.35
Cedar Key	17.65	17.18	0.47	30.89	31.51	−0.62
St. Petersburg	15.50	15.76	−0.26	38.70	41.57	−2.87
Naples	13.97	16.35	−2.38	3.07	13.20	−10.13
Key West	9.40	9.97	−0.57	−7.80	−5.35	−2.45
			K_1			
South Pass	14.01	13.38	0.63	17.63	25.82	−8.19
Waveland	15.93	16.35	−0.42	62.84	60.76	2.08
Pensacola	13.63	13.72	−0.09	51.85	48.40	3.45
Panama	13.99	13.64	0.35	36.25	27.11	9.14
Apalachicola	12.70	13.35	−0.65	51.60	48.24	3.36
Cedar Key	21.86	19.98	1.88	34.60	39.04	−4.44
St. Petersburg	16.60	16.46	0.14	50.50	51.67	−1.17
Naples	15.24	14.95	0.29	8.93	17.31	−8.38
Key West	9.02	8.88	0.14	−3.90	−6.62	2.72

$$r(\tau) = \frac{R(\tau)}{\sigma_\eta \sigma_u}, \tag{2}$$

where $R(\tau) = E[\eta(t)u(t + \tau)]$; σ_η and σ_u are the standard deviation for η and u, respectively; and τ is the time lag. The time lags determined for the composite are similar to the time lags found for M_2 constituent alone (Table 3a), reiterating the dominance of the M_2 constituent on the WFS.

3. Hydrodynamic model

Our work is preceded by several numerical model studies of Gulf of Mexico tides. Reid and Whitaker (1981) applied a finite-difference version of the linearized Laplace tidal equations in a two-dimensional 15′ by 15′ (~28 km) horizontal grid to portray the barotropic response of the Gulf of Mexico to tidal forcing. While describing the deep water tides well, their coarse

TABLE 2. Normalized rms tidal residuals showing the contributions of nontidal fluctuations to the sea level variability at the nine tide gauges spanning the study domain.

Gauge	South Pass	Waveland	Pensacola	Panama City	Apalachicola	Cedar Key	St. Petersburg	Naples	Key West
$\frac{\sigma_r}{\sigma_0}$%	70.88	74.74	70.76	71.03	70.64	50.71	57.24	47.14	56.41

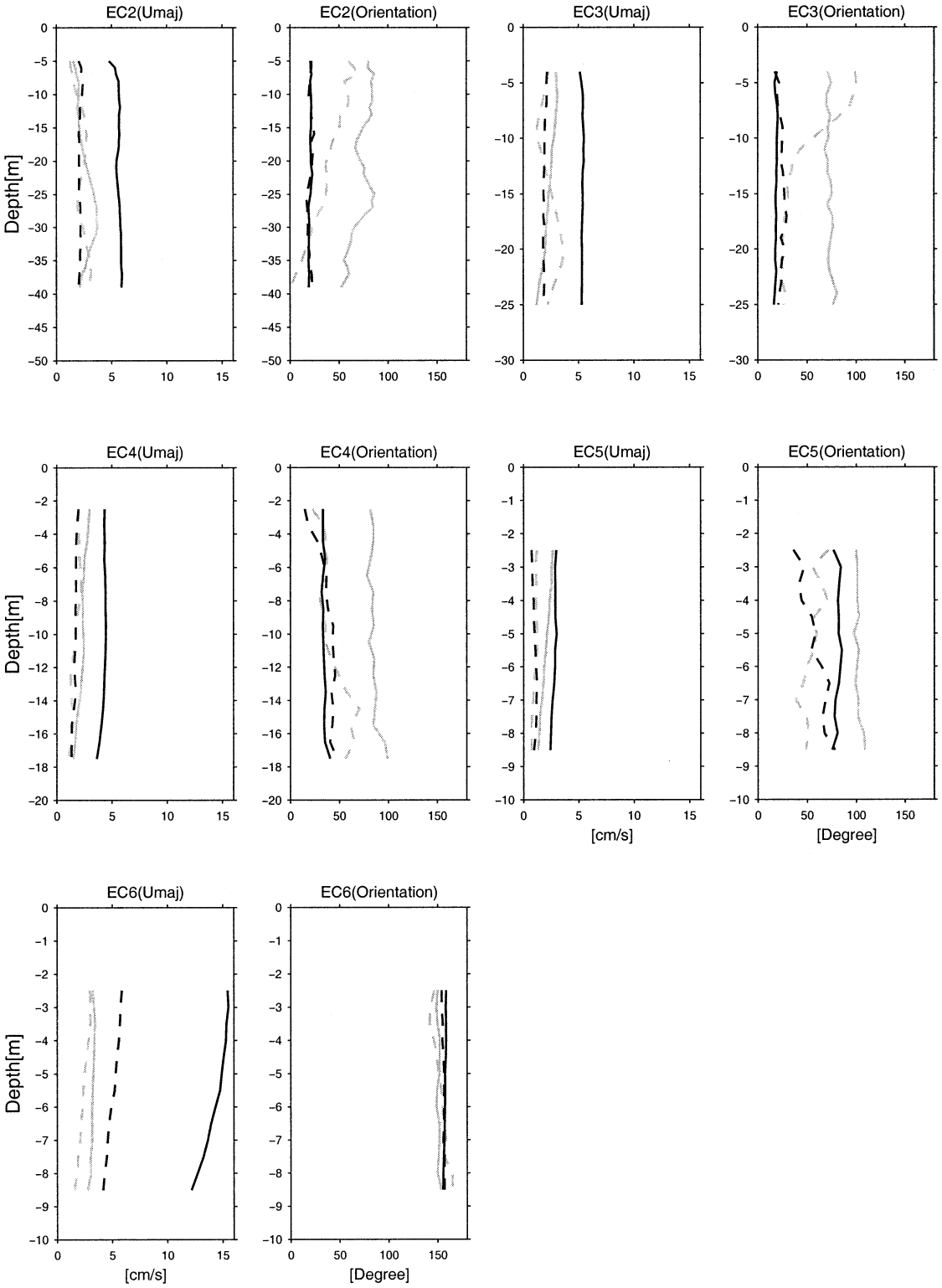

FIG. 2. Vertical profiles of the velocity hodograph ellipses semimajor axis amplitudes and orientations (measured anticlockwise from east) for the EC designated moorings. The thick solid and dashed lines denote M_2 and S_2, respectively. The thin solid and dashed lines denote O_1 and K_1, respectively.

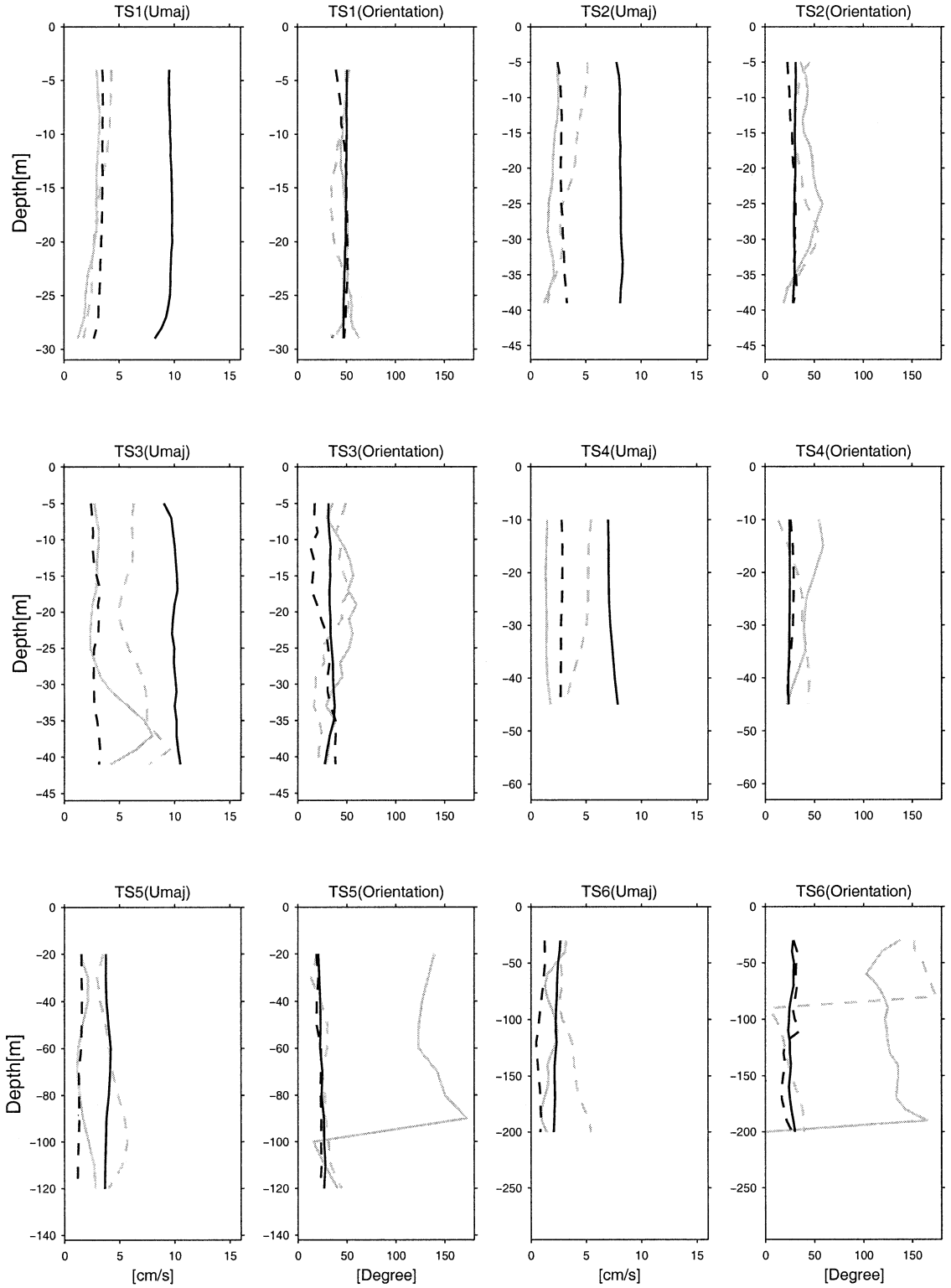

FIG. 3. Vertical profiles of the velocity hodograph ellipse semimajor axis amplitudes and orientations (measured anticlockwise from east) for the TS designated moorings. The thick solid and dashed lines denote M_2 and S_2, respectively. The thin solid and dashed lines denote O_1 and K_1, respectively.

TABLE 3a. Greenwich phases of the major tidal constituents at the St. Petersburg tide gauge and at the 12 ADCP stations (left-hand columns), plus the relative times between high water at St. Petersburg and maximum (shoreward directed) semimajor axis tidal currents at the 12 ADCP stations (right-hand columns). Phase differences are converted to time differences using speeds of M_2, S_2, O_1 and K_1 of 29.98 deg h^{-1}, 30.00 deg h^{-1}, 13.94 deg h^{-1} and 15.04 deg h^{-1}, respectively, where "+" and "−" indicate time lags and leads, respectively.

	M_2		S_2		O_1		K_1	
Station	(deg)	(h)	(deg)	(h)	(deg)	(h)	(deg)	(h)
St. Petersburg	198.10	0.00	216.10	0.00	38.70	0.00	50.50	0.00
AS1	148.80	−1.70	123.81	−3.07	23.26	−1.10	311.92	17.38
TS1	51.39	−5.06	70.41	−4.86	269.34	16.54	262.49	14.09
TS2	21.39	−6.10	33.37	−6.09	250.58	15.19	237.69	12.44
TS3	63.57	−4.64	84.84	−4.37	246.39	14.89	280.66	15.30
TS4	52.08	−5.04	69.01	−4.90	239.42	14.39	250.05	13.26
TS5	54.16	−4.97	68.94	−4.90	261.06	15.95	241.93	12.72
TS6	53.56	−4.98	69.73	−4.87	322.91	20.38	208.68	10.51
EC2	45.17	−5.27	58.13	−5.26	260.83	15.93	286.86	15.71
EC3	47.09	−5.21	56.72	−5.31	256.08	15.59	284.58	15.56
EC4	20.35	−6.13	40.23	−5.86	226.26	13.45	270.08	14.59
EC5	−9.64	−6.93	33.71	−6.07	221.70	13.12	275.70	14.97
EC6	−93.69	−9.76	−106.10	−10.74	159.10	8.63	139.98	5.94

grid size was insufficient to describe the tidal structures on the shelf. Westerink et al. (1993) applied a finite-element-based hydrodynamic model (ADCIRC-2DDI), also depth integrated and two-dimensional, to the western North Atlantic, the Gulf of Mexico, and the Caribbean Sea, to develop a tidal constituent database. Computations were presented for varying horizontal resolutions ranging from coarse (1.6° × 1.6°) to fine (6′ × 6′), and discussion was given to the importance of model resolution. Their model comparisons with sea level data show good agreements in the Atlantic Ocean, but persistent errors occurred in the Gulf of Mexico and the Caribbean Sea. These authors suggested that insufficient resolution over the continental shelf, particularly in the shallowest regions, might be responsible for the relatively poor numerical convergence in those regions. More recently, L. Kantha et al. (2002, personal communication; material available online at http://www.ssc.erc.msstate.edu/Tides2D/) developed a data-assimilative, barotropic tidal model for the Gulf of Mexico with similar grid resolution as Reid and Whitaker (1981). Improved results follow from the assimilation of selected coastal tide gauge data. Nevertheless, this model has insufficient resolution to describe the structure of the tidal variations on the WFS.

Our approach is therefore a regional one. The hydrodynamic model used is the Princeton Ocean Model (POM), a three-dimensional, nonlinear, primitive equation model with Boussinesq and hydrostatic approximations (Blumberg and Mellor 1987). The model uses an orthogonal curvilinear coordinate system in the horizontal and a sigma

$$\left(\sigma = \frac{z - \eta}{\eta + H}\right)$$

coordinate system in the vertical, where z is the conventional vertical coordinate (positive upward from zero at the mean water level), H is the local water depth, and η is the tidal variation about the mean water depth. Our model domain (Fig. 4) extends from the Mississippi River in the northwest to the Florida Keys in the southeast, with one open boundary that arcs between these two locations. Horizontal resolution varies from less than 2 km near the coast to about 6 km near the open boundary, and the minimum water depth is set at 2 m. This grid allows us to resolve the complicated features of the coastline and the isobath geometries in order to explore the associated structures of the WFS tides. We use 21 sigma layers in the vertical with higher resolution near the bottom to better resolve the frictional boundary dynamics. Bottom stress is obtained by a quadratic drag law in which a nondimensional drag coefficient is calculated on the basis of a specified (0.01 m) bottom roughness length. The model has a total of 121 × 81 × 21 grid points, and the time step for the external mode is 12 s.

Water density is assumed homogeneous in this three-dimensional barotropic tide study. The three-dimensional distribution of the vertical eddy viscosity is computed using the Mellor and Yamada (1982) level-2.5 turbulence closure scheme, and the horizontal eddy viscosity is calculated using the shear-dependent Smagorinsky formulation (Smagorinsky 1963) with a coeffi-

TABLE 3b. The time lags between high tide at St. Petersburg and the maximum (shoreward directed) semimajor axis tidal currents at the 12 ADCP stations determined by the maximum lag-correlation coefficient between the composites of the M_2, S_2, O_1, and K_1 constituents.

Station	St. Petersburg	AS1	TS1	TS2	TS3	TS4	TS5	TS6	EC2	EC3	EC4	EC5	EC6
Time lag (h)	0.00	−2.31	−5.53	−6.45	−5.25	−5.18	−5.65	−5.68	−5.77	−5.86	−6.36	−7.37	−8.16

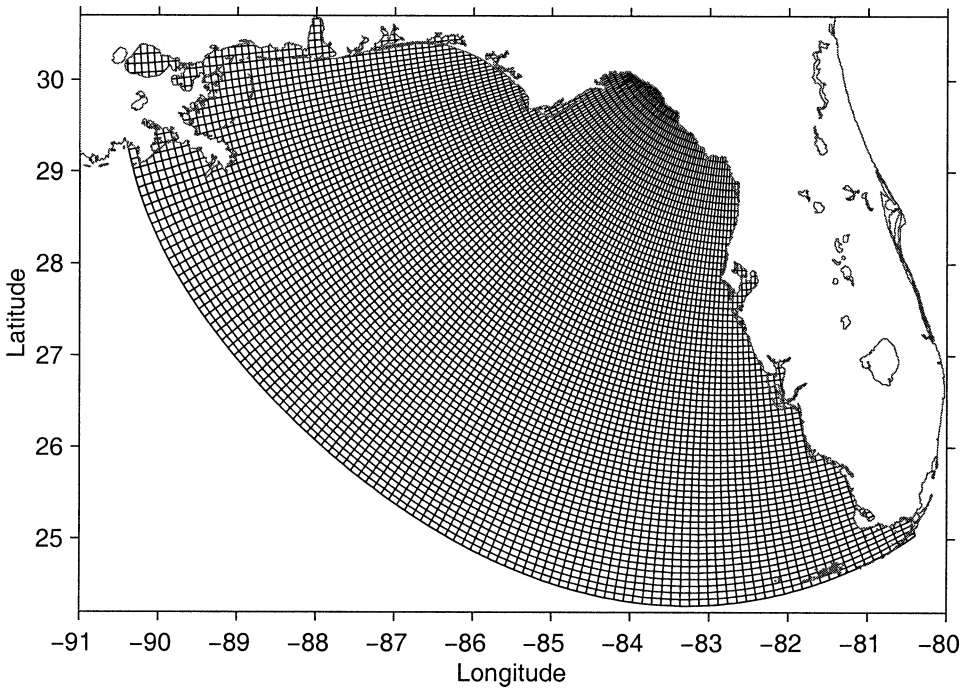

FIG. 4. The model grid used for the regional tidal simulation.

cient of 0.2. Dissipation by vertical friction is found to largely exceed that by horizontal friction.

The bathymetry adopted in the model begins with the World Ocean Elevation Data ETOPO5 5′ × 5′ global bathymetry dataset. Since this dataset is inaccurate in the southern portion of WFS we corrected it by incorporating data from NOAA navigation charts and National Geophysical Data Center (NGDC) bathymetry contours. Our modified bathymetry has been used in other WFS modeling studies with satisfactory results (e.g., He and Weisberg 2002; Weisberg et al. 2001; Yang et al. 1999).

Tidal forcing of the model is exclusively at the open boundary. There, the tidal elevations are specified by a linear interpolation of the output from the TOPEX/Poseidon data assimilated global tidal model of Tierney et al. (2000). This barotropic model, with 15′ resolution, provides eight tidal constituents (M_2, S_2, N_2, K_2, K_1, O_1, P_1, and Q_1) over a nearly global domain that extends from 80°S to 66°N. The model assimilates both coastal tide gauge data and ocean tides derived from four years of TOPEX/Poseidon satellite altimetry data. Since it uses procedures that tend to preserve the spatial tidal structures in shallow water, it is considered to be a suitable product for forcing higher-resolution regional tidal models. Figure 5 shows the distributions of tidal amplitudes and phases for M_2, S_2, K_1, and O_1 constituents along the open boundary where we have a total of 121 model grids.

4. Modeled elevations and currents

a. General features

The model is forced at the open boundary by specifying the composite M_2, S_2, K_1, and O_1 constituent elevations there. Elevations, currents, and turbulence quantities are computed over the model interior by integrating forward in time beginning from a state of rest. An initial spinup period of five inertial cycles (about five days) is used to suppress transients. The subsequent 30 days are then analyzed using the same techniques as for the in situ data to retrieve individual constituent amplitude and phase distributions over the model domain. Table 1 provides amplitude and phase comparisons between the modeled and observed elevations of M_2, S_2, K_1, and O_1 at the nine coastal tide gauge stations spanning the analysis domain. Amplitude differences are generally less than 2 cm; the singular exception being at Cedar Key where it is 2.5 cm for M_2. Phase differences are generally less than 10°; with Naples at 10.1° for O_1 being the largest. Both amplitude and phase differences show equally likely plus or minus values demonstrating that the modeled tides are not biased. Root-mean-square (rms) values of the phase differences, when converted to time, amount to less than 10 min (20 min) for the semidiurnal (diurnal) species. Considering the model tide gauge sampling relative to the actual tide gauge positions and the nearshore masking (2 m being the shallowest model depth), these phase agreements are

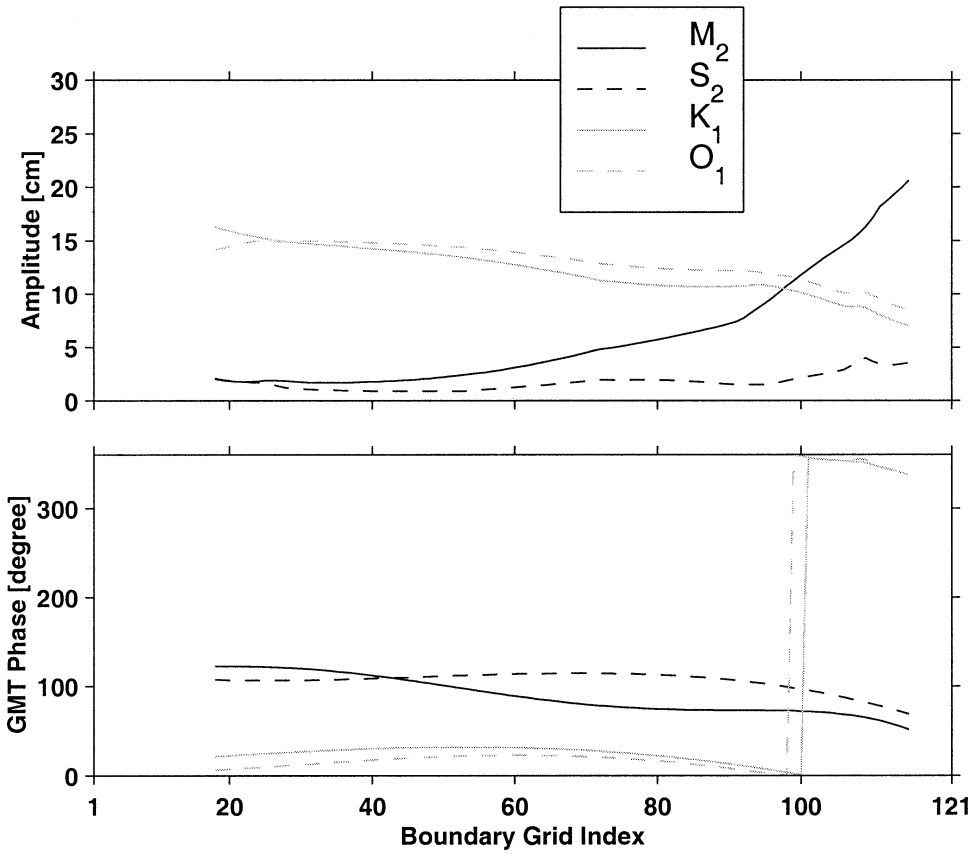

FIG. 5. The distributions of tidal (top) amplitudes and (bottom) phases along the model open boundary for the M_2, S_2, K_1, and O_1 constituents (see legend provided). The abscissa is the grid index that includes both points over land and water. The land points are masked, and so only the points over water are shown.

both good and as good as can be expected. Therefore, no model tuning was considered.

The alongcoast variations of the amplitudes and phases of the four major tidal constituents are graphically shown in Fig. 6, where circles denote the observations and crosses indicate the model results. Allowing for scale changes in the abscissa we see a relative spatial homogeneity in the diurnal species compared with a more spatial inhomogeneous distribution for the semidiurnal species. We also note several bull's-eyes in the model–observation comparison.

The agreements of Table 1 and Fig. 6 justify using the model to produce coamplitude and cophase charts for the M_2, S_2, O_1, and K_1 constituents (Fig. 7). In general agreement with the findings of the previously cited Gulf of Mexico tide studies, these maps provide further details of the tidal structures on the WFS. The semidiurnal and diurnal species are distinctly different. The phase of the M_2 tide advances toward the northwest. Apalachicola Bay separates the M_2 tidal regime into two parts. To the west the M_2 tide is weak. To the east it is strong. Both the Florida Big Bend and the Florida Bay regions show relative maxima with a relative minimum in between just to the south of Tampa Bay. The S_2 constituent shows features similar to the M_2 constituent, but with a much smaller amplitude. The phase patterns for the semidiurnal species appear to result by diffraction around the Florida Keys and onto Cape San Blas.

Amplification of the semidiurnal tides in the Florida Big Bend has been discussed by previous investigators. Reid and Whitaker (1981) considered a resonance deriving from the counterclockwise speed of propagation matching the group speed for a gravest mode edge wave (gS/f where S is the bottom slope—Kajiura 1958). With these speeds in close alignment and with the M_2 tide wrapping around the basin approximately once per tidal cycle, near resonance may be achieved (these authors estimated an average M_2 propagation speed of 98 m s^{-1} and an edge wave speed of 120 m s^{-1}). While this type of resonance is possible, we note that bottom topography and edge wave speeds vary around the shelf as does the M_2 tide amplitude and phase gradient.

Local geometry may also induce amplification. The isobath (Fig. 1) and the coamplitude plots for the semidiurnal tides (Fig. 7) show similarity. Where the shelf is narrow the amplitudes are small, and conversely. The two regions of widest shelf are the Florida Big Bend and Florida Bay with a relative minimum in between,

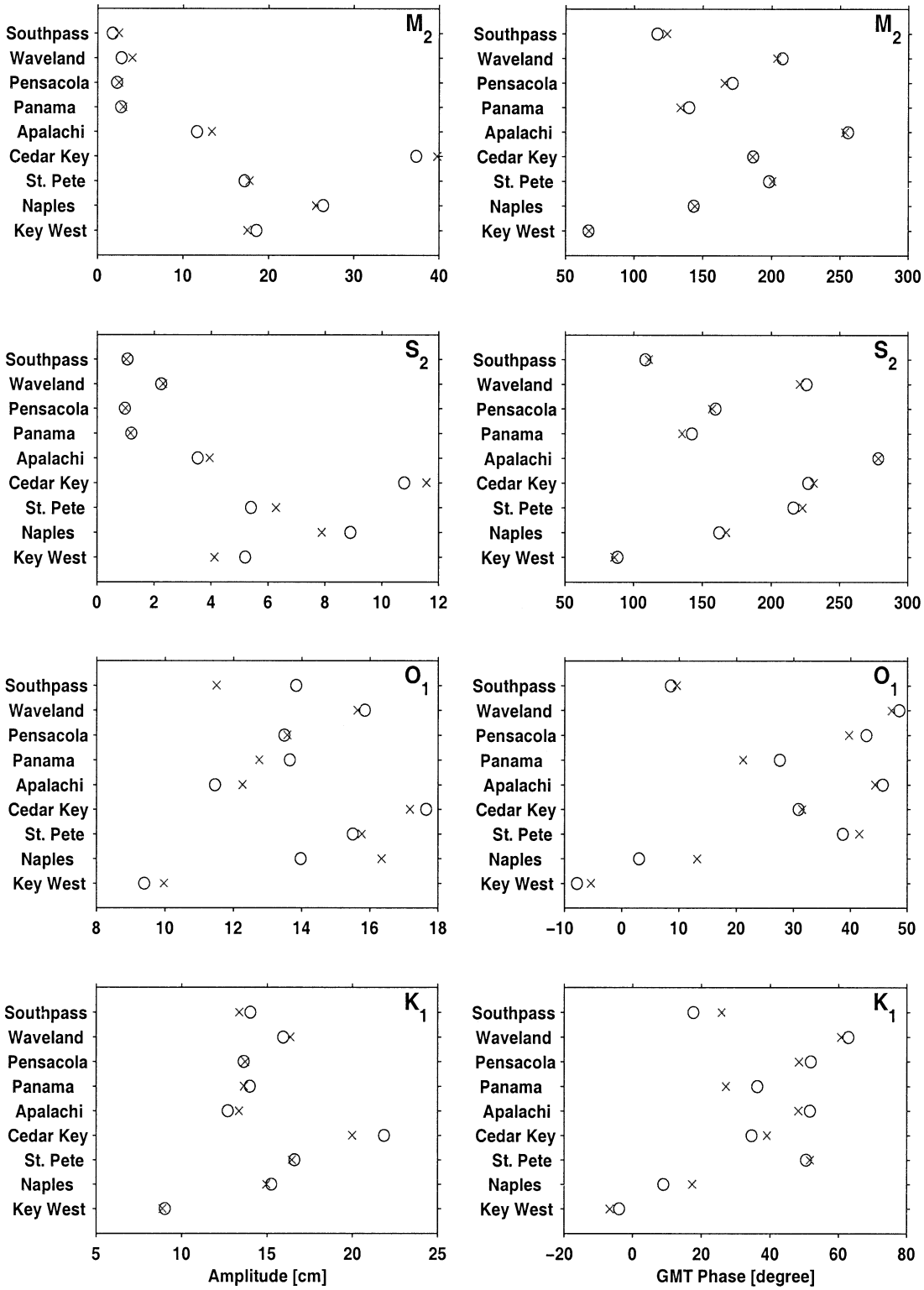

FIG. 6. Comparisons between modeled and observed (left) amplitudes and (right) Greenwich phases for the M_2, S_2, K_1, and O_1 constituents at the nine coastal tide gauge locations. Crosses (circles) denote modeled (observed) values. Bull's-eyes are where they overlay.

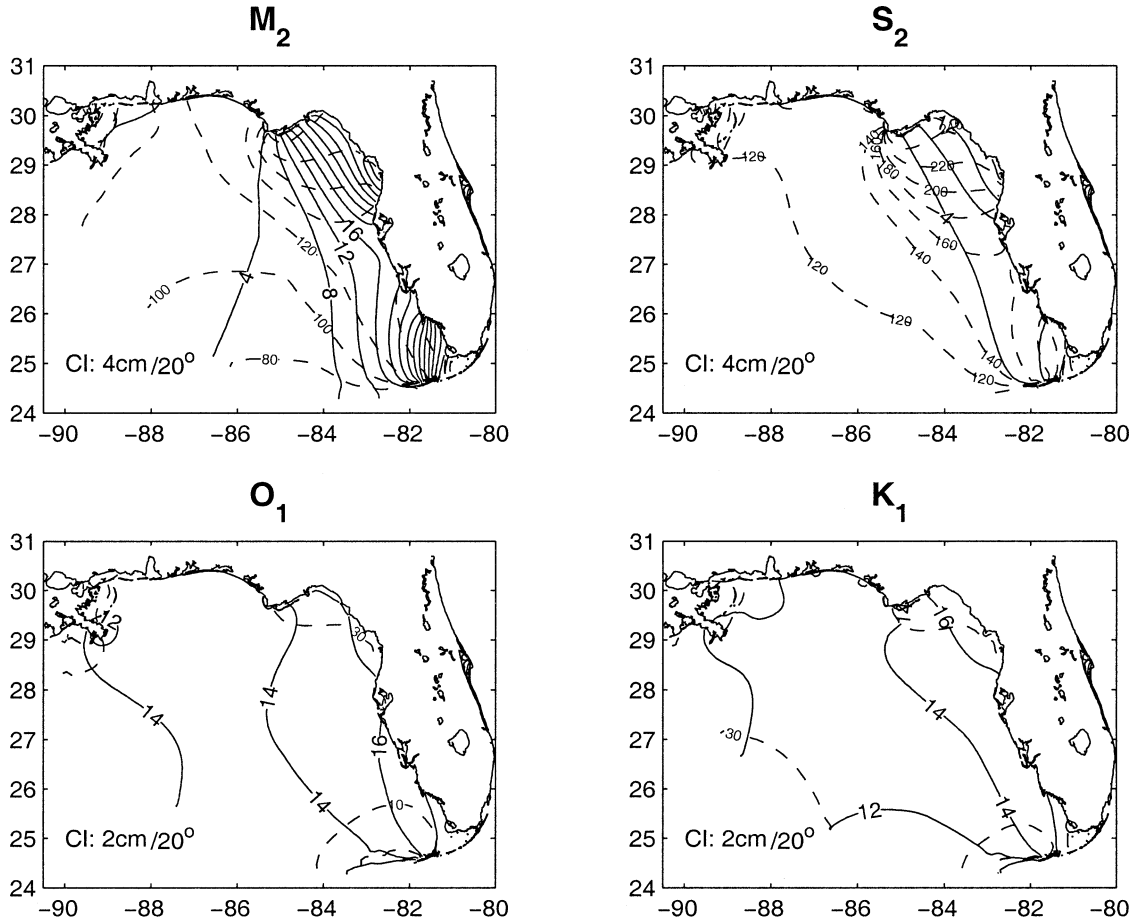

FIG. 7. Modeled coamplitude and cophase (relative to the Greenwich meridian) distributions for the M_2, S_2, O_1, and K_1 tidal constituents. Solid (dashed) lines denote amplitudes (phases), and the contour intervals are indicated in the lower-left corner of each panel.

as reflected in the coamplitude distributions. Effects of local geometry are considered in the analytical treatments of Battisti and Clarke (1982a,b) and Clarke (1991). For a continental shelf with an along-shore scale much greater than the shelf width these authors developed a one-dimensional tide model to explain some of the observed barotropic tidal characteristics. Using a linearized bottom stress (ru/h), the linear Laplace tidal equations are

$$\left(\frac{\partial}{\partial t} + \frac{r}{h}\right)u - fv = -g\eta_x,$$

$$\left(\frac{\partial}{\partial t} + \frac{r}{h}\right)v + fu = -g\eta_y. \tag{3}$$

For tidal motions over a continental shelf with constant slope α and width a, that is, $h(x) = \alpha x$, $0 \le x \le a$, they expressed sea level in terms of a zero order Bessel function as

$$\frac{\eta(a)}{\eta(0)} = J_0[2(\mu a)^{1/2}],$$

where

$$\mu a \approx \left(\frac{\omega^2 - f^2}{g\alpha}\right)a. \tag{4}$$

For the semidiurnal tide ($\omega^2 - f^2 > 0$) on a wide shelf (a/α is large), $\mu a \to 1$ and $\eta(a)/\eta(0) \to 0$, implying amplification of semidiurnal tides across a wide shelf. To account for alongshore variations in the tides, Lentz et al. (2001) developed an analytical, flat-bottom, two-dimensional model with varying shelf width. These analytical models are both consistent with the observed semidiurnal tide behaviors on the WFS. They suggest that the coamplitude distributions may be the result of local geometry, as contrasted with the previous basin-scale resonance arguments.

Unlike the semidiurnal tides, the diurnal tides show little coamplitude variations across the analysis domain. Both amplitudes and phases for the O_1 and K_1 constituents are nearly spatially uniform. This is consistent

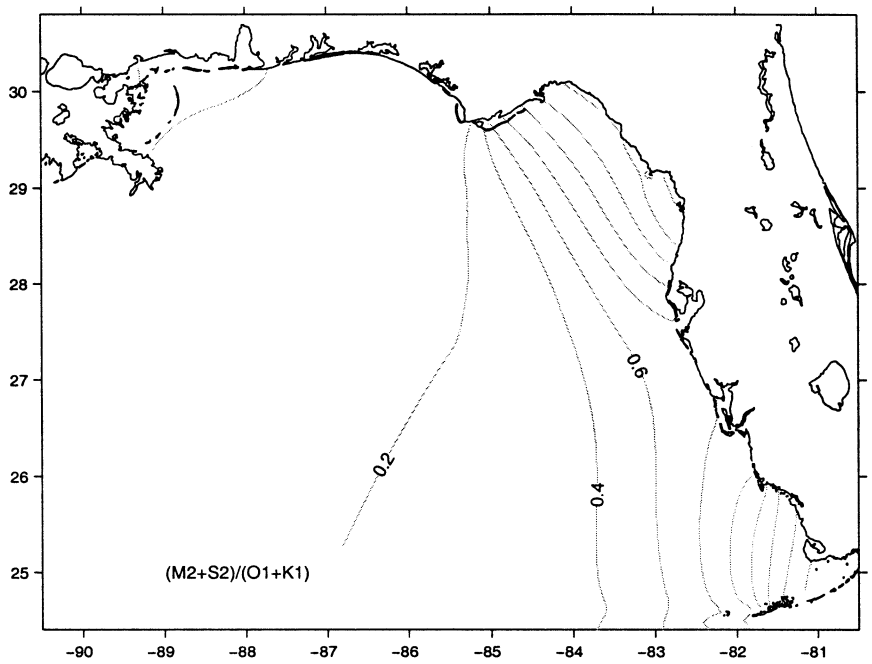

FIG. 8. The amplitude ratio between the principal semidiurnal and diurnal tides.

with the Zetler and Hansen (1971) finding that the diurnal tide is essentially in phase throughout the Gulf of Mexico. It is also consistent with Eq. (4) (Clarke 1991), since for $\omega \approx f$ on the WFS, $\mu a \to 0$, so the diurnal tides do not amplify toward the coast. The O_1 and K_1 constituents also have comparable amplitudes with mean ratio of 0.95. Basin-scale resonance for these constituents is not expected because their propagation speeds are about half those of the semidiurnal constituents, so they do not circumscribe the basin within a tidal period as do the semidiurnal species (R. Reid 2001, personal communication).

The ratio between the amplitudes of the principal semidiurnal and diurnal tide constituents, $(M_2 + S_2)/(K_1 + O_1)$, is shown in Fig. 8. While the WFS tidal regime is generally characterized as mixed and mainly of diurnal type, this is not true of the inner half of the WFS where the ratio exceeds 0.5 and especially of the Florida Big Bend and Florida Bay regions where the semidiurnal tides dominate. It is only over the outer portion of the WFS and to the west of Apalachicola Bay where the diurnal species dominate.

Given the model sea level descriptions and the model and in situ data agreements for sea level at the coast, we now examine the tidal currents in a similar manner. Figure 9 compares the depth-averaged tidal current hodographs (calculated for all of the in situ data locations of Fig. 1) with the depth-averaged tidal current hodographs calculated from the model, sampled at all of these in situ data sites. Qualitatively, the comparisons are very good for the semidiurnal constituents with ellipse semimajor amplitudes, eccentricities, and orientations all in agreement (see Table 4 for listings of the hodograph ellipse semimajor axes, semiminor axes, and orientations). Particularly notable is how the ellipse orientations diverge away from the region of relative minimum semidiurnal tide elevation just south of Tampa Bay. Eccentricities at the stations close to the coast show the largest departures between the data and the model, which may be a consequence of the model turbulence parameterization. Deviations from an inviscid fluid semiminor to semimajor axis ratio of ωf^{-1} are due to the friction, which is consistent with the largest departures being in the shallowest water. Nevertheless, the agreements are still very good. The overall agreements between the observed and modeled diurnal constituents, while also good, are degraded somewhat from those of their semidiurnal brethren, and there are additional reasons for this behavior.

As pointed out by Reid and Whitaker (1981), modeled currents are more sensitive to factors such as bottom friction, horizontal eddy diffusivity, and topography than are modeled water levels. A particular problem in the Gulf of Mexico for diurnal constituents is the closeness in frequency between these and the local inertial period. Large inertial oscillations exist in the WFS observations when the water column is stratified. While not a subject of this paper, we did investigate several different techniques in attempting to minimize inertial oscillation interference in the data. For instance, we broke the data records into month-long pieces to distinguish barotropic tides during months without stratification versus mixed barotropic tides and inertial oscillations during months with stratification. Nonuniform modulation made this too subjective, however. Recognizing that the inertial oscillations when present are pre-

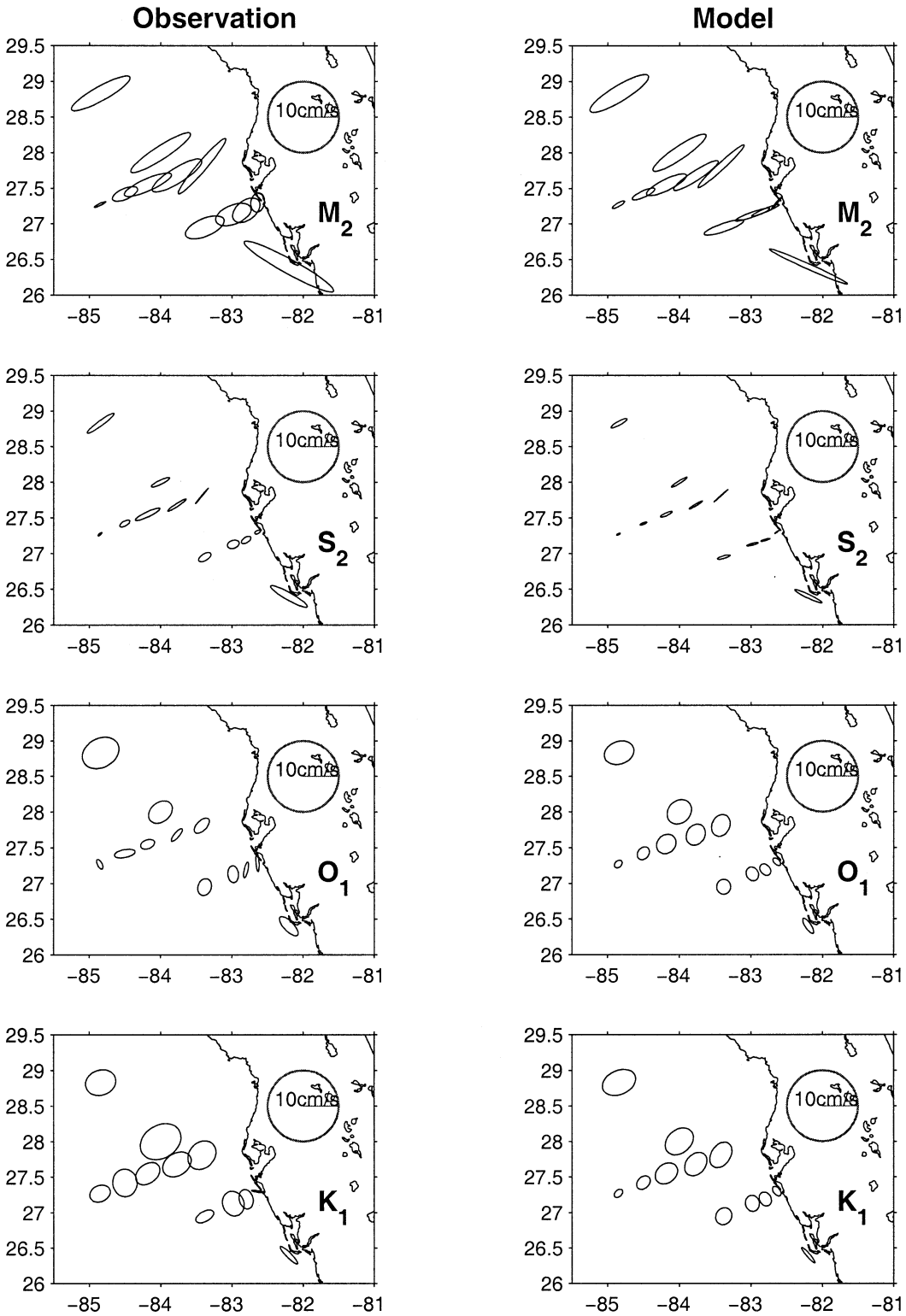

FIG. 9. A comparison between the (left) observed and (right) modeled M_2, S_2, O_1, and K_1 tidal current hodograph ellipses at the 12 moored ADCP locations.

TABLE 4. A comparison of computed and observed tidal ellipse parameters.

	Semimajor ($\times 10^{-2}$ m s^{-1})		Semiminor ($\times 10^{-2}$ m s^{-1})		Orientation (deg)	
	Observed	Modeled	Observed	Modeled	Observed	Modeled
			M_2			
AS1	9.38	9.52	−2.01	−2.22	29.05	31.34
TS1	10.21	8.78	−1.30	−0.97	49.52	42.98
TS2	8.12	7.38	−2.14	−1.34	31.94	33.26
TS3	9.95	8.92	−1.84	−1.79	32.99	34.29
TS4	7.21	6.19	−1.70	−1.57	23.95	26.37
TS5	3.83	3.49	−1.52	−0.89	24.05	25.06
TS6	1.79	1.96	−0.28	−0.49	25.64	29.58
EC2	5.82	5.84	−2.48	−1.12	23.05	18.93
EC3	5.24	5.07	−2.68	−0.70	22.13	19.71
EC4	4.40	4.15	−2.71	−0.49	30.58	22.73
EC5	2.75	2.22	−1.92	−0.49	79.44	59.75
EC6	14.35	12.01	−2.03	−1.03	151.08	155.76
			S_2			
AS1	4.65	2.55	−0.71	−0.54	35.88	29.47
TS1	2.81	2.63	−0.09	−0.05	50.48	41.37
TS2	3.08	2.16	−0.41	−0.26	33.04	30.87
TS3	2.82	2.57	−0.58	−0.36	26.17	32.13
TS4	3.83	1.80	−0.70	−0.38	25.43	24.02
TS5	1.60	1.01	−0.66	−0.24	29.46	22.93
TS6	0.70	0.56	−0.21	−0.15	38.61	28.17
EC2	1.98	1.86	−0.93	−0.37	21.30	15.94
EC3	1.69	1.63	−1.12	−0.25	18.88	14.96
EC4	1.52	1.34	−0.75	−0.20	22.38	16.47
EC5	0.86	0.68	−0.44	−0.17	26.32	35.76
EC6	5.91	4.23	−1.03	−0.52	150.65	154.71
			O_1			
AS1	5.44	4.27	−4.08	−3.18	29.44	20.81
TS1	2.68	3.17	−1.40	−2.49	64.88	65.88
TS2	2.25	3.08	−0.69	−2.51	49.19	58.98
TS3	3.71	3.72	−2.69	−3.08	39.13	45.84
TS4	2.06	2.93	−1.24	−2.50	40.48	46.56
TS5	2.95	1.95	−1.09	−1.53	40.78	51.05
TS6	1.47	1.24	−0.66	−0.88	65.52	44.82
EC2	2.43	2.10	−1.87	−1.95	70.87	86.65
EC3	2.38	2.01	−1.50	−1.64	105.01	117.00
EC4	2.27	1.79	−0.51	−1.32	103.83	129.66
EC5	2.63	1.30	−0.43	−0.74	106.65	137.52
EC6	3.50	2.53	−1.36	−0.81	134.03	132.82
			K_1			
AS1	4.34	4.93	−3.49	−3.32	19.12	24.44
TS1	4.38	3.90	−3.53	−2.70	50.56	57.05
TS2	4.34	3.65	−3.09	−2.68	40.14	49.93
TS3	6.11	4.41	−4.61	−3.24	32.49	41.59
TS4	3.80	3.40	−2.64	−2.64	38.58	39.43
TS5	3.87	2.19	−3.41	−1.60	55.58	44.20
TS6	3.00	1.38	−2.27	−0.91	23.79	41.98
EC2	2.77	2.47	−1.41	−2.18	38.07	54.62
EC3	3.53	2.26	−2.97	−1.95	112.20	100.32
EC4	2.75	2.03	−1.94	−1.60	105.56	119.29
EC5	1.74	1.56	−0.23	−0.90	141.99	129.42
EC6	3.44	2.83	−0.69	−0.33	134.64	130.94

dominantly of first baroclinic mode structure we opted to perform the data analyses on depth-averaged currents, effectively averaging out the inertial oscillations. Nevertheless, some nontidal inertial oscillatory behavior may still be contaminating the diurnal constituent hodographs of Fig. 9. Similar problems do not exist for the semidiurnal constituents since they are removed in frequency from the inertial oscillations. Some amplification is observed in the data during months when the WFS is stratified, but this is small relative to the barotropic tides. Whether such amplification is the result of internal tide generation or a reduction in the effects of bottom friction by the stratification remains to be determined.

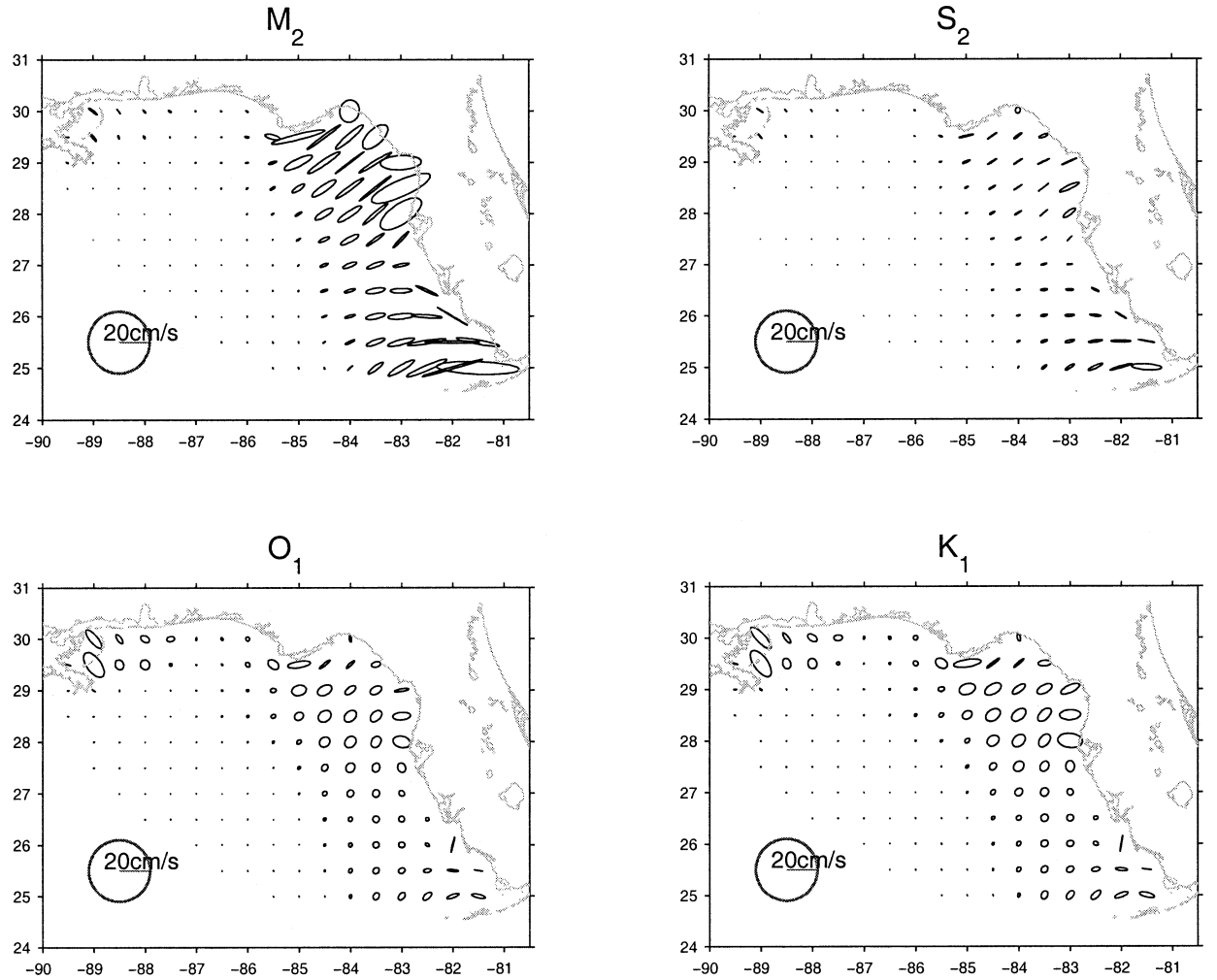

FIG. 10. The distributions over the entire model domain of the modeled M_2, S_2, O_1, and K_1 tidal current hodograph ellipses.

The agreements between the observed and modeled tidal current ellipses are sufficiently good to warrant the mapping of these ellipses over the entire model domain. These are shown in Fig. 10 for the M_2, S_2, O_1, and K_1 constituents. The general patterns seen in the coamplitude contours are reflected here. The M_2 currents amplify from very small values in deep water to largest values (approaching 20 cm s^{-1}) near shore in the Florida Big Bend and Florida Bay. The relative minimum in between to the south of Tampa Bay is evident with the hodograph orientations diverging away from this point. To the west of Apalachicola Bay we see very little M_2 tidal current except just to the east of the Mississippi River where the shelf again widens away from the DeSoto Canyon. The S_2 tidal currents behave very similarly to the M_2 tidal current except that they are weaker. The O_1, and K_1 ellipses appear very similar to one another, being weaker than the M_2 and stronger than the S_2 ellipses over the WFS, but stronger than either of these to the west of Apalachicola Bay. Eccentricities in general agree with the tendencies from inviscid theory that the tidal ellipses should be more circular (ωf^{-1}) for the diurnal species than for the semidiurnal species, and the polarizations are clockwise.

b. *Tidal residual current and the Lagrangian transport*

The model, being fully nonlinear, is capable of generating responses in addition to the four linear tidal harmonics with which it is forced. Here we investigate these tidal residual currents (U_{res}, V_{res}) defined as the difference between the model responses (U, V) and the four constituent tidal harmonic currents analyzed from the model output. Thus, the Eulerian residual current is calculated as

$$U_{\text{res}} = U - \sum u_i \cos(\sigma_i t - \alpha_i)$$
$$V_{\text{res}} = V - \sum v_i \cos(\sigma_i t - \beta_i), \qquad (5)$$

where (u_i, v_i) and (α_i, β_i) are the analyzed harmonic constants for the M_2, S_2, K_1 and O_1 tidal constituents.

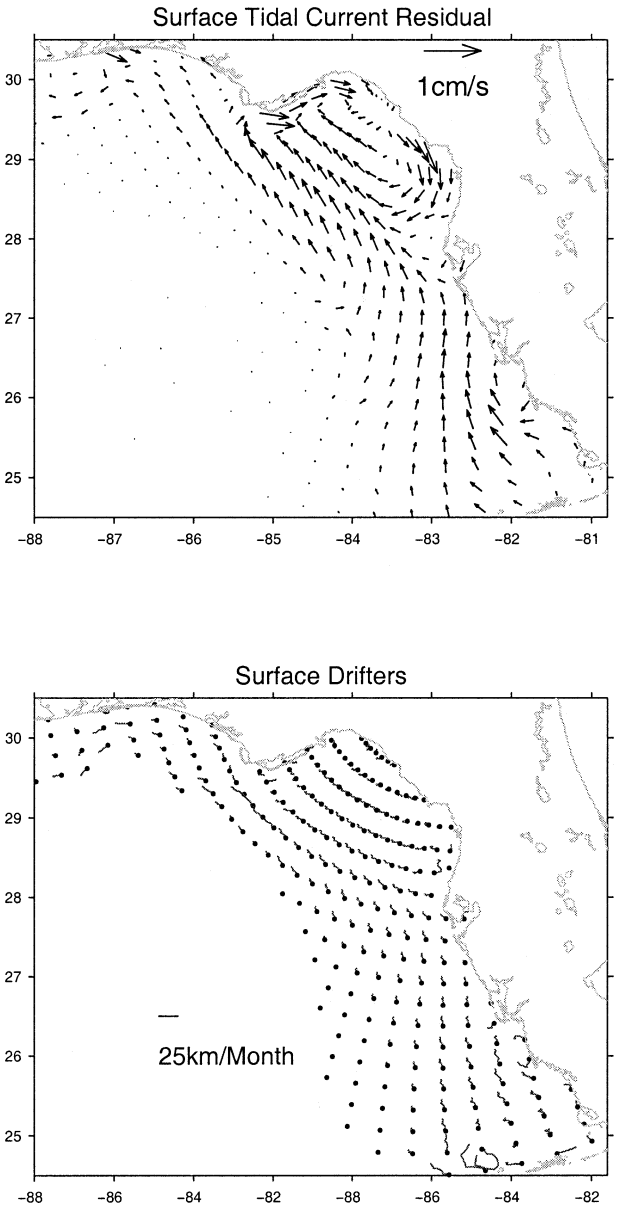

FIG. 11. (top) Eulerian and (bottom) Lagrangian representations of the tidal residual surface circulation.

Figure 11 presents the residual currents in both Eulerian and Lagrangian frameworks. The Eulerian representation (upper panel) is the residual surface current field after subtracting from each grid point the linear least squares fit of the four major tidal constituents. The Eulerian residual field is weak (generally less than 0.01 m s^{-1}) and generally directed toward the north or northwest consistent with the propagation direction for the semidiurnal tides. Vectors appear largest in the Florida Big Bend where they also form an anticyclonic gyre. The Lagrangian representation (lower panel) is calculated by tracking surface drifters originating at every fourth grid point over a 30-day period; that is, they are Lagrangian trajectories for dynamically passive particles released at the surface on day 6 (after the five day spinup period) and tracked through day 35. The patterns appear very similar to the Eulerian representation. Particle displacements are small (order 10 km $month^{-1}$) suggesting that barotropic tidal current rectification is not a mechanism of major importance in transporting materials on the WFS.

5. Bottom stress and turbulence mixing

Turbulence mixing in this POM-based barotropic tide model derives from bottom stress calculated using a quadratic drag law. Here we examine the bottom stress distribution, its mixing ramifications for the water column, and the implications of these findings for simpler models that employ a linear drag law. For simplicity, only the M_2 current is considered since it is the dominant contributor to the WFS tidal currents.

Bottom stress, for either depth-dependent or depth-averaged models, may be defined in several different ways, such as

$$\tau_b = \rho u_*^2 = \rho C_D |u| u = \rho r \overline{u}, \tag{6}$$

where ρ is the water density and for the first two (depth-dependent) cases, u_* is the friction velocity, C_D is a bottom drag coefficient, and u is the near-bottom current. For the third (depth averaged) case $\overline{u}$ is the depth-averaged current and r is a resistance coefficient. For our application, we consider the rms value of τ_b calculated over 10 M_2 tidal cycles from which the friction velocity u_* is obtained as $(\tau_b/\rho)^{1/2}$. A map of this u_* for the WFS M_2 tide is given in the upper panel of Fig. 12. The spatial variations of u_* or the magnitude of turbulence mixing reflects the spatial variations in the tidal current magnitude. Regions of the largest tidal mixing are associated with regions of the strongest tidal currents found in relatively shallow water. In particular the maximum values of u_* (greater than 0.36 cm s^{-1}) are found in the Florida Big Bend and in Florida Bay.

Since bottom stress is calculated by a quadratic drag law, it is of interest to check the sensitivity of our results to the bottom drag coefficient C_D. The adjustable parameter in

$$C_D = \max\left\{0.0025, \left[\frac{1}{k}\ln\left(\frac{1+\sigma_b}{z_0/D}\right)\right]^{-2}\right\} \tag{7}$$

is the bottom roughness length z_0. The default value for z_0 is 0.01 m. For sensitivity studies we ran a series of model experiments in which we varied z_0 between 0.002 and 0.05 m and found no significant differences in model performance. We then replaced Eq. (7) with a smaller spatially uniform drag coefficient ($C_D = 0.001$). This substantial change in drag coefficient, especially in shallow water, resulted in a disproportionately small change in the model response. In analogy to a damped harmonic oscillator, where proportionately small (large) increases

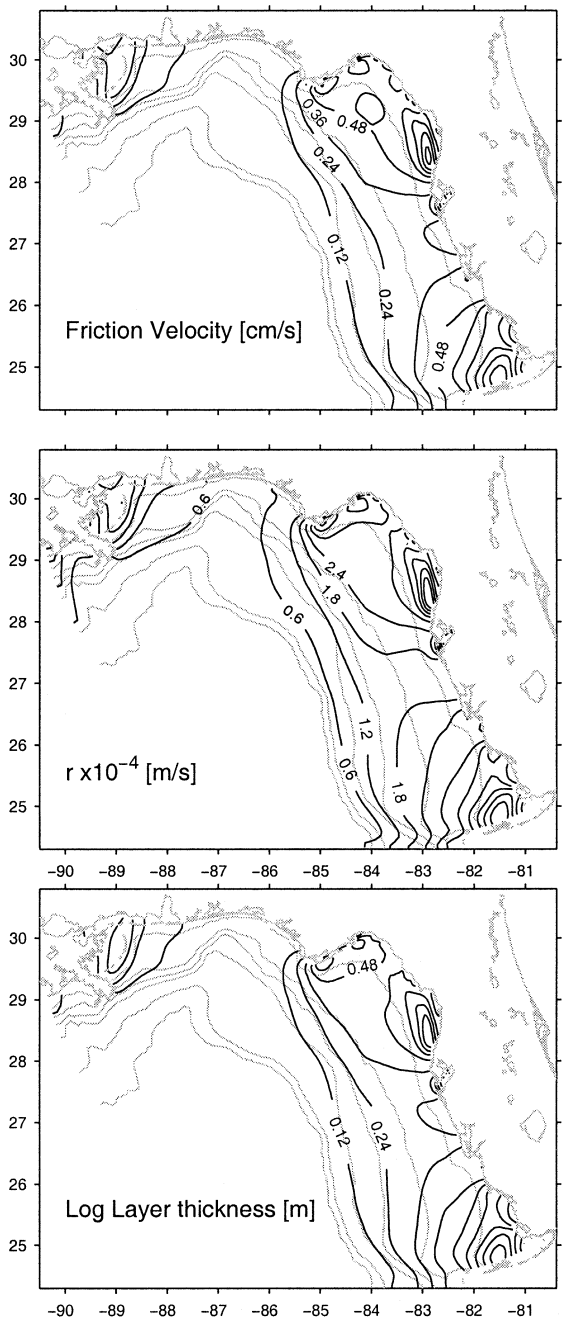

FIG. 12. The spatial distribution of mixing properties inferred from the M_2 tidal currents. From the top to bottom are the friction velocity (u_*), the resistance coefficient (r), and the log-layer thickness. Units are provided in each panel, as are bathymetric contours (light lines) for isobaths 20, 50, 100, 200, 1000, and 2000 m.

in response occur away from (near)resonance, our sensitivity findings suggest that tidal amplifications in the Big Bend and Florida Bay regions are nonresonant, supporting the earlier assertion that geometry is the cause of the observed amplification.

For the case of linear, depth-averaged models bottom stress is set by the resistance coefficient r. As examples, Clarke (1991) used $r = 2 \times 10^{-4}$ m s^{-1}, whereas Lentz et al. (2001) found $r = 5 \times 10^{-4}$ m s^{-1} to be appropriate for the North Carolina shelf. Using rms bottom stress and depth-averaged current distributions we arrive at r estimations here [Eq. (6)] that range across the shelf from 0.6 to 6 ($\times 10^{-4}$ m s^{-1}) (middle panel of Fig. 12). Thus, the use of constant values for r, while appealing for linear model calculations, may either overestimate or underestimate the bottom stress on continental shelves. Value judgements about quadratic versus linear drag laws, aside, we simply emphasize that bottom friction parameterization for models remains a complex, empirical issue.

Boundary layer theory identifies different layers (e.g., Soulsby 1983) each with different behaviors. The ''bed layer'' immediately adjacent to the bottom is where molecular viscosity ν controls the dynamics. Within this layer (of a few centimeters thickness) we have

$$\rho\nu \frac{d\overline{U}}{dz} = \tau = \tau(0) = \rho u_*^2 \quad \text{or} \quad \frac{U}{u_*} = \frac{u_* z}{\nu}. \tag{8}$$

Above the bed layer is the ''logarithmic layer'' within which neither the details of the bed nor the free-stream flow affect the local dynamics, and for which the velocity profile follows the universal form,

$$\frac{\overline{U}}{u_*} = \frac{1}{k} \ln \frac{z}{z_0}, \tag{9}$$

where $k \approx 0.4$ is the von Kármán constant.

Above the logarithmic layer is the ''outer layer'' for which the velocity and turbulence profiles depend on the nature of flow and hence obviates universality.

Defining an eddy viscosity A (e.g., Wimbush and Munk 1970) as

$$\tau = \rho(A + \nu) \frac{d\overline{U}}{dz}, \tag{10}$$

noting that $A \gg \nu$ where the constant stress and logarithmic regions overlap and using Eqs. (8) and (10), we arrive at

$$A = cu_* z. \tag{11}$$

By similarity we can use this specification for A to estimate the Ekman layer thickness δ for steady-state flow regimes; that is,

$$f\overline{U} = \frac{\partial}{\partial z}\left(A \frac{\partial \overline{U}}{\partial z}\right) = cu_* \frac{\overline{U}}{\delta} \Rightarrow \delta = c \frac{u_*}{f}, \tag{12}$$

where f is the local Coriolis parameter and $c = 0.1$–0.4 (e.g., Loder and Greenberg 1986; Weatherly and Martin 1978).

Oscillatory boundary layers require further analysis if the local acceleration becomes of equal or greater importance as the Coriolis acceleration. Introducing the complex current, $W = u + iv$, into the momentum equations,

$$\frac{\partial u}{\partial t} - fv = \frac{\partial}{\partial z}\left(A\frac{\partial u}{\partial z}\right), \quad \frac{\partial u}{\partial t} + fu = \frac{\partial}{\partial z}\left(A\frac{\partial v}{\partial z}\right), \qquad (13)$$

and assuming $W \propto e^{i\sigma t}$, where σ is the frequency of oscillation, we arrive at [in analogy to Eq. (12)]

$$i(\sigma + f)W = \frac{\partial}{\partial z}\left(A\frac{\partial W}{\partial z}\right) \propto cu_*\frac{W}{\delta} \Rightarrow |\delta| = \frac{cu_*}{(\sigma + f)}. \qquad (14)$$

For the case of the M_2 tide-induced bottom boundary layer on the WFS, with $\sigma_{M_2} \approx 2f$, the bottom boundary layer thickness may be estimated as $\delta \approx cu_*/(3f)$. Using a midrange value of $c = 0.2$, the bottom boundary thickness induced by the M_2 tidal current over most of the WFS is estimated at about 2–5 m (except near Cedar Key and in Florida Bay where it is comparable to the water depth). Therefore, tidal mixing alone is insufficient to mix the water column on the WFS.

The height of the logarithmic layer is taken as some fraction of the Ekman depth. Soulsby (1983), for instance, defines the logarithmic layer height as 0.1δ and with this definition the lower panel of Fig. 12 shows the M_2 tidal-current-induced logarithmic layer height for the WFS. Values are generally less than 1 m. Empirical determinations of the log layer based on the in situ bottom boundary layer measurement on the WFS are presently in progress and these will be reported on separately.

6. Summary

Using in situ data and a numerical circulation model we examine the structure of the WFS tides and the effects of the tides in distributing water properties and in mixing the water column vertically. Attention is limited to barotropic tides and to the four major tidal constituents (M_2, S_2, O_1, and K_1) that account for the bulk of the tidal variance (~90%) of the region. The data are from coastal sea level stations ranging from the Mississippi River delta to the Florida Keys, and from current meter moorings deployed across the shelf between the 10-m and 300-m isobaths. The model is a regional adaptation of the POM extending from west of the Mississippi River to the Florida Keys with a single open boundary arcing between these land termini. Regional tides are produced by forcing the model at its open boundary using the composite M_2, S_2, O_1, and K_1 sea level variability from the global (TOPEX/Poseidon assimilated) tide model of Tierney et al. (2000). With standard tidal analysis tools, we produce coamplitude and cophase maps for each constituent and compare both sea level and currents against actual observations. Based on the fidelity of comparison we then use the model products to discuss the WFS barotropic tides.

Apalachicola Bay, in the Florida Panhandle, is a dividing point between appreciable semidiurnal tides to the east over the WFS and minimal semidiurnal tides from there to the Mississippi River delta. In contrast with the semidiurnal tides, the diurnal tides are spatially more uniform. With respect to overall rms sea level variability, tides account for about 30% west of, versus about 50% southeast of Apalachicola Bay, respectively. The balance of the rms variability is due to synoptic scale weather-induced sea level change. Coamplitude maps show largest tides in the regions where the shelf is widest, that is, in the Florida Big Bend and in Florida Bay. The region just south of Tampa Bay shows a relative minimum. Both the amplification of the semidiurnal constituents and the spatial variations with shelf width are consistent with linear theory (e.g., Clarke 1991; Lentz et al. 2001). Such theory also accounts for the relative spatial uniformity of the diurnal constituents. We conclude that the spatial distributions of the tides on the WFS are the result of local geometry, as contrasted with previous ideas about basinwide tidal resonance.

The tidal currents on the WFS, especially the semidiurnal constituents, are primarily barotropic. Very good agreements are obtained between the in situ data derived and the modeled tidal hodograph ellipses. Semimajor axes are generally less than 0.1 m s^{-1}, and the ellipses are generally oriented normal to the shoreline. Ellipse orientation, however, does reflect the coamplitude distributions with tidal currents tending to diverge (converge) on regions of relative minima (maxima). A relatively small seasonal modulation is observed in the semidiurnal tidal currents due to either internal tides or reductions in friction by stratification. Larger seasonal modulation is observed in the diurnal constituents due to the generation of inertial oscillations under stratified conditions. Inertial oscillations, when present, are generally organized as first baroclinic modes, so they tend to cancel out when performing vertical averages. This helps to facilitate the barotropic tidal analyses. Baroclinic tides and inertial oscillations will be reported on separately.

The nonlinearity of the model allows it to generate mean currents despite its linear harmonic forcing. We present these residual currents in both Eulerian and Lagrangian frameworks to assess their potential effects on tidal residual material transports. While a coherent Stokes-drift pattern toward the northwest emerges, the magnitudes are small (one to two orders of magnitude less than the semimajor axis speeds) amounting to net particle trajectories of generally less than 10 km per month. Albeit persistent, this is smaller than the potential particle trajectories for either seasonal or synoptic scale forcing (e.g., Weisberg et al. 1996).

With the M_2 tide having the largest tidal current magnitude we use this constituent to examine the spatial distribution of bottom stress by tides on the WFS and the role that this may play in water column mixing. Except for the shallow regions of the Florida Big Bend

and Florida Bay, the potential for mixing by tides is weak. Attempting to parameterize friction in a linear model using a resistance coefficient is limited by the spatial variability in bottom stress; nevertheless, the values estimated are within the range of values used in other studies. Estimates of logarithmic layer thickness by the M_2 tide are generally less than 1 m and empirical studies are under way to quantify this better.

In closing, with quantifiable metrics we show that regional tides on the WFS may be adequately described by forcing a regional, primitive equation, three-dimensional model with a global tide model at the open boundary, and that the properties of the tidal variations result primarily from the local geometry.

Acknowledgments. The in situ data collection and numerical model developments benefited from several sponsors. The measurements were initiated under a cooperative agreement between the U.S. Geological Survey, Center for Coastal Geology and the USF College of Marine Science. Subsequent support by the Minerals Management Service, Cooperative Agreement 14-35-0001-30787, is noted. Our work continues under support by the Office of Naval Research Grant N00014-98-1-0158 and the National Oceanic and Atmospheric Administration Grant NA76RG0463. Special thanks are offered to the family of Elsie and William Knight for the research fellowship endowment that helped to support R. He. Messrs. R. Cole, J. Donovan, and C. Merz are largely responsible for the success of the field program. Dr. S. Meyers contributed analyses and discussions, and we are particularly grateful for the helpful e-mail discussions provided by Prof. Robert Reid. The sensitivity test on the drag coefficient in section 5 was at the suggestion of an anonymous reviewer.

REFERENCES

Battisti, D. S., and A. J. Clarke, 1982a: A simple method for estimating barotropic tidal currents on continental margins with specific application to the M_2 tide off the Atlantic and Pacific coasts of the United States. *J. Phys. Oceanogr.*, **12,** 8–16.

——, and ——, 1982b: Estimation of nearshore tidal currents on nonsmooth continental shelves. *J. Geophys. Res.,* **87,** 7873–7878.

Blumberg, A. F., and G. L. Mellor, 1987: A description of a three-dimensional coastal ocean circulation model. *Three-Dimensional Coastal Ocean Models,* N. Heaps, Ed., Vol. 4, Amer. Geophys. Union, 208–233.

Clarke, A. J., 1991: The dynamics of barotropic tides over the continental shelf and slope (review). *Tidal Hydrogynamics,* B. Parker, Ed., John Wiley and Sons, 79–108.

Foreman, M. G. G., 1978: Manual for tidal currents analysis and prediction. Pacific Marine Science Rep. 78-6, Institute of Ocean Science, Patricia Bay, Sidney, BC, Canada, 70 pp.

——, and R. F. Henry, 1979: Tidal analysis based on high and low water observations. Pacific Marine Science Rep. 79-15, Institute of Ocean Science, Patricia Bay, Sidney, BC, Canada, 39 pp.

Godin, G., 1972: *The Analysis of Tides.* University of Toronto Press, 264 pp.

Grace, S. F., 1932: The principle diurnal constituent of tidal motion in the Gulf of Mexico. *Mon. Not. Roy. Astron. Soc. Geophys.*, **3** (Suppl.), 70–83.

He, R., and R. H. Weisberg, 2002: West Florida shelf circulation and temperature budget for the spring transition, 1999. *Cont. Shelf Res.,* **22,** 719–748.

Kajiura, K., 1958: Effect of Coriolis force on edge waves. (II) Specific examples of free and forced waves. *J. Mar. Res.*, **16,** 145–157.

Koblinsky, C. J., 1981: The M_2 tide on the West Florida Shelf. *Deep-Sea Res.,* **28A,** 1517–1532.

Lentz, S., M. Carr, and T. H. Herbers, 2001: Barotropic tides on the North Carolina shelf. *J. Phys. Oceanogr.*, **31,** 1843–1859.

Loder, J. W., and D. A. Greenberg, 1986: Predicted positions of tidal fronts in the Gulf of Maine region. *Cont. Shelf Res.,* **6,** 394–414.

Marmorino, G. O., 1983: Variability of current, temperature, and bottom pressure across the West Florida continental shelf, winter 1981–1982. *J. Geophys. Res.,* **88** (C7), 4439–4457.

Mellor, G. L., and T. Yamada, 1982: Development of a turbulence closure model for geophysical fluid problems. *Rev. Geophys.*, **20,** 851–875.

Reid, R. O., and R. E. Whitaker, 1981: Numerical model for astronomical tides in the Gulf of Mexico. Texas A&M Rep. for U.S. Army Engineers Waterway Experiment Station, 115 pp.

Smagorinsky, J., 1963: General circulation experiments with primitive equations. I. The basic experiment. *Mon. Wea. Rev.,* **91,** 99–164.

Soulsby, R. L., 1983: The bottom boundary layer of shelf seas. *Physical Oceanography of Coastal and Shelf Seas,* B. Johns, Ed., Oceanography Series, Vol. 35, Elsevier, 189–266.

Tierney, C. C., L. H. Kantha, and G. H. Born, 2000: Shallow and deep water global ocean tides from altimetry and numerical modeling. *J. Geophys. Res.,* **105,** 11 259–11 277.

Weatherly, G. L., and P. Martin, 1978: On the structure and dynamics of the oceanic bottom boundary layer. *J. Phys. Oceanogr.,* **8,** 557–570.

Weisberg, R. H., B. D. Black, and H. Yang, 1996: Seasonal modulation of the West Florida continental shelf circulation. *Geophys. Res. Lett.,* **23,** 2247–2250.

——, Z. Li, and F. Muller-Karger, 2001: West Florida shelf response to local wind forcing, April 1998. *J. Geophys. Res.,* **106** (C12), 31 239–31 262.

Westerink, J. J., R. A. Luettich, N. Scheffner, 1993: ADCIRC: An advanced three-dimensional circulation model for shelves, coast, and estuaries. Report 3: Development of a tidal constituent database for the western North Atlantic and Gulf of Mexico. Tech. Rep. DRP-92-6, U.S. Army Corps of Engineers, 154 pp.

Wimbush, M., and W. H. Munk, 1970: The benthic boundary layer. *The Sea,* M. N. Hill, Ed., New Concepts of Sea Floor Evolution. Part I: General Observations, Vol. 4, Wiley and Sons, 731–758.

Yang, H., R. H. Weisberg, P. P. Niiler, W. Sturges, W. Johnson, 1999: Lagrangian circulation and forbidden zone on the West Florida Shelf. *Cont. Shelf Res.,* **19,** 1221–1245.

Zetler, B. D., and D. V. Hansen 1971: Tides in the Gulf of Mexico. *Contributions on the Physical Oceanography of the Gulf of Mexico,* Vol. 2, L. R. A. Capurro and J. L. Reid, Eds., Gulf Publishing, 265–275.